Research Article | Vol. 32, No. 7 / 25 Mar 2024 / Optics Express 11474
Optics EXPRESS

Temporally optimized and spectrally shaped hyperspectral coherent anti-Stokes Raman scattering microscopy

LINGXIAO YANG,[1,2] RISHYASHRING R. IYER,[1,2] JANET E. SORRELLS,[1,3] CARLOS A. RENTERIA,[1,3] AND STEPHEN A. BOPPART[1,2,3,4,5,6,*]

[1]Beckman Institute for Advanced Science and Technology, University of Illinois Urbana-Champaign, Urbana, IL 61801, USA
[2]Department of Electrical and Computer Engineering, University of Illinois Urbana-Champaign, Urbana, IL 61801, USA
[3]Department of Bioengineering, University of Illinois Urbana-Champaign, Urbana, IL 61801, USA
[4]NIH/NIBIB Center for Label-free Imaging and Multiscale Biophotonics, University of Illinois Urbana-Champaign, Urbana, IL 61801, USA
[5]Cancer Center at Illinois, University of Illinois Urbana-Champaign, Urbana, IL 61801, USA
[6]Interdisciplinary Health Sciences Institute, University of Illinois Urbana-Champaign, Urbana, IL 61801, USA
*boppart@illinois.edu

Abstract: Coherent anti-Stokes Raman scattering (CARS) microscopy offers label-free chemical contrasts based on molecular vibrations. Hyperspectral CARS (HS-CARS) microscopy enables comprehensive microscale chemical characterization of biological samples. Various HS-CARS methods have been developed with individual advantages and disadvantages. We present what we believe to be a new temporally optimized and spectrally shaped (TOSS) HS-CARS method to overcome the limitations of existing techniques by providing precise control of the spatial and temporal profiles of the excitation beams for efficient and accurate measurements. This method uniquely uses Fourier transform pulse shaping based on a two-dimensional spatial light modulator to control the phase and amplitude of the excitation beams. TOSS-HS-CARS achieves fast, stable, and flexible acquisition, minimizes photodamage, and is highly adaptable to a multimodal multiphoton imaging system.

1. Introduction

Coherent anti-Stokes Raman scattering (CARS) microscopy is a label-free optical imaging technique that provides chemical contrasts based on molecular vibrations. Arising from a third-order multiphoton light-matter interaction, the CARS signal is orders of magnitude stronger than that from spontaneous Raman scattering, and, thus, the signals can be acquired at higher speeds for microscopy [1–3]. CARS employs near-infrared ultrashort excitation pulses that allow intrinsic optical sectioning and increased penetration depth, which enables thick tissue imaging for three-dimensional microscopy. The blue-shifted CARS signals can easily be separated from the excitation pulses and additional light-matter interactions such as fluorescence or harmonic generation using spectral filters. Developments in the last two decades have made CARS a ubiquitous tool for chemical, physical, and biological sciences for material characterization, biochemical profiling of the tissue microenvironment, disease diagnostics, and drug assessments [4–7].

In CARS, a pump beam (ω_p) and a Stokes beam (ω_s) with a frequency difference equal to the Raman vibrational frequency of a molecule $\Omega_R = \omega_p - \omega_s$, generate an anti-Stokes signal at a new frequency $\omega_{as} = 2\omega_p - \omega_s$. Development of computational methods, such as the Kramers-Kronig

#517417 https://doi.org/10.1364/OE.517417
Journal © 2024 Received 2 Jan 2024; revised 15 Feb 2024; accepted 16 Feb 2024; published 13 Mar 2024

Optics EXPRESS

(KK) phase retrieval and detrending, have enabled the removal of the unwanted non-resonant background (NRB) to enable CARS as a ubiquitous tool for high-resolution and accurate spectral characterization [8–10]. Single-frequency CARS microscopy, where the pump and Stokes beam frequencies are tuned to probe a single vibrational frequency, is relatively straightforward to implement but has limited specificity, and provides minimal chemical information. Hyperspectral CARS (HS-CARS) microscopy is essential for a more comprehensive chemical characterization of samples and for visualization of this chemical information at the microscale [1–3]. The spectral and temporal characteristics of the pump and Stokes beams dictate the speed, tunability, and efficiency of CARS generation. Precise control of the spectral and temporal profiles of the beams can yield more versatile CARS techniques for new applications.

There have been various implementations of HS-CARS that can be broadly categorized as being multiplexed or sequential scanning-based techniques. In multiplexed HS-CARS, a broadband Stokes beam is compressed in time and interacts with a narrowband pump. The CARS spectrum is recorded by a spectrometer at each pixel [11–14]. Although each spectrum at each pixel can be acquired within a few milliseconds, the frame duration scales up significantly with the number of pixels for microscopy applications. The two prevalent methods of sequential scanning-based HS-CARS use narrowband beams for both pump and Stokes. The first method is through direct laser wavelength tuning, achieved using tunable lasers [15,16] or optical parametric oscillators (OPO) [17,18]. HS-CARS using either technology requires quickly tuning the temporal delay between the pump and Stokes beams for each vibrational frequency by either mechanical [16,18] or electronic means [15] These often-customized lasers and OPOs are not readily accessible to researchers, and are difficult to be adapted into commercial or multimodal imaging platforms. A more popular method for sequential scanning for HS-CARS is spectral focusing, where the pulses in both the pump and Stokes beams are chirped and stretched to picosecond pulse widths. Different frequencies of Raman vibrations can be probed by tuning the temporal overlap of the two beams [19,20]. There are several limitations of this spectral focusing method. First, temporal delay tuning usually involves mechanical movements from piezoelectric-driven stages or scanning mirrors. These electromechanical elements can be unstable due to hysteresis and cause misalignment of the two beams between or within imaging sessions. Rigorous and regular calibration is needed to map the optical path length difference to the vibrational frequency difference to avoid distortions to the recorded CARS spectra. Second, since the two beams are only partially overlapped in time for any single vibrational frequency, the excitation power is not efficiently used to generate the CARS signals, which can exacerbate the photodamage to biological samples. Third, since the overlap between the pump and Stokes is not uniform, the detected spectra are bounded by an envelope function that further constricts the range.

In all these methods, precise control of the spatial and temporal profiles is essential to obtain efficient and accurate measurements with good spectral resolution. Generally, the best spectral resolution in scanning-based HS-CARS is achieved when the slopes of the time bandwidth of the pump and the Stokes beam are linear and identical. The beam dispersion is commonly controlled using elements such as fiber brag gratings, prism pairs, chirped mirrors, or glass rods [15–20]. These elements are limited to compensating only second-order dispersion and have limited tunability. Fourier transform pulse shaping (FTPS) has been a well-recognized technique for manipulating the temporal and spectral properties of laser pulses, usually with a diffraction grating and a spatial light modulator (SLM) in a 4-f configuration [21]. Traditionally, SLMs in pulse shapers only have a linear array of pixels made of liquid crystals (LCs) for one-dimensional (1D) control of the spectral profile [21,22]. Two-dimensional (2D) SLMs have gained increasing prevalence in the market, have higher pixel density compared to their 1D counterparts, and are generally 10 times more affordable than a commercial FTPS. Both 1D and 2D SLMs can modulate the spectral phase of input pulses. However, 1D SLMs modulate the amplitude of each spectral bin using polarization modulation with respect to the SLM LC axis which also affects

Optics EXPRESS

the efficiency of phase modulation [23]. Independent amplitude control can be achieved with two serial layers of 1D SLMs at a cost of increased power loss and added dispersion artifacts [23]. In contrast, independent amplitude modulation by 2D SLMs achieves higher power efficiency using diffraction-based methods [23–25]. Amplitude modulation using 2D SLMs has been used in various applications, such as optical metrology [26], quantum optics [27,28], and optical processing [29], and has been made commercially available. Two-dimensional SLMs have been integrated into commercial FTPS devices for the optimization of multiphoton excitation by compensating the spectral phase distortions of the imaging systems to achieve transform-limited femtosecond pulses at the sample plane [30,31]. In Raman spectroscopy, 2D SLMs have been used for beam steering and compressive detection [32,33] and there have been some studies using 1D phase masks to enable single beam excitation [34,35], multiplexing [36], and spectrally tailored excitation [37]. To the best of our knowledge, the ability of 2D SLMs to perform independent spectral phase and amplitude modulations has not been used to sequentially scan spectral components with temporal optimizations for high-speed HS-CARS microscopy.

In this paper, we propose a new method to perform HS-CARS, called temporally optimized and spectrally shaped HS-CARS (TOSS-HS-CARS), with quick, versatile, and independent spectral and temporal tunability using a Fourier-transform pulse shaper with a 2D-SLM that overcomes the limitations of existing scanning-based HS-CARS techniques. In TOSS-HS-CARS, a spectrally broadband pulse (~2000cm^{-1}) is obtained at either the pump or the Stokes bands using supercontinuum generation, whose amplitude and phase are then tuned independently for every spectral sub-band (10-20 cm^{-1}) using the 2D-SLM-based FTPS, based on the application and upon interaction with the other beam. This method does not involve any mechanically moving elements, minimizes photodamage by modulating and utilizing the incident pulse energy efficiently, and achieves stable operation at high speed. It also affords wide tunability to various spectral resolutions and bands, provides flexible acquisition schemes, and can be readily integrated into a multimodal imaging system that incorporates a single commercially available laser source.

Figure 1(a) shows the time-frequency distributions of the proposed TOSS-HS-CARS method, with comparisons to the existing common HS-CARS methods of spectral focusing (SF), broadband (BB), and direct laser scanning (LS). We also include a qualitative comparison of their exposure utility, speed, stability, and adaptability (Fig. 1(b)) based on the literature [11–18]. Exposure utility describes the percentage of incident power (both pump and Stokes) that contributes to the CARS signal generation. The discussion of speed here pertains specifically to the acquisition rate of a data cube containing the spectrum for each pixel in an image. The stability metric refers to the ability to get repeatable HS measurements within and across imaging sessions. Adaptability describes the flexibility in acquisition methods, ranges of Raman frequencies, and the ability to be integrated into a multimodal platform. In TOSS-HS-CARS, either the pump or the Stokes can be spectrally shaped to match the pulse width and frequency bandwidth of the other beam. High-fidelity phase modulation is used to minimize the dispersion mismatch of the two-color beams, while high-efficiency amplitude modulation is used to perform sub-nanometer wavelength selection and tuning. Pulse shaping ensures complete temporal overlap of the two beams, which indicates high exposure utilization, and stable operation during fast tuning. Unlike SF, where both the pump and Stokes beams are narrowband and chirped, TOSS-HS-CARS can operate for various pulse-width regimes (picosecond to femtosecond). Additionally, the time-frequency distribution of the two beams in SF and LS HS-CARS are empirically assumed to be the same (i.e., identical ellipses in the diagram). However, this is challenging practically without the pulse shaper due to higher-order dispersion. Furthermore, the partial temporal overlap in SF-HS-CARS also means poor utilization of the optical energy exposed to the samples. In the following sections, we describe two possible configurations of TOSS-HS-CARS with pulse shapers for either the pump or Stokes beams (Fig. 1(c)) for characterizing different chemical compounds and

Optics EXPRESS

lipid-protein contents in biological samples. We also detail a simple and comprehensive series of steps to design, calibrate, and operate a 2D FTPS device for tunable HS-CARS microscopy.

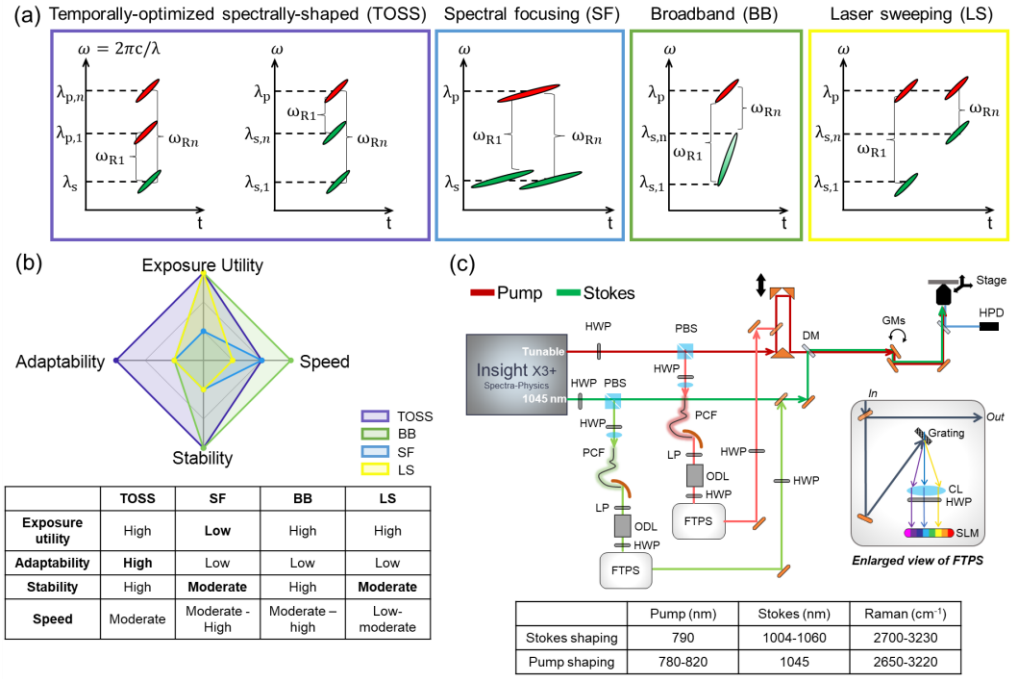

	TOSS	SF	BB	LS
Exposure utility	High	**Low**	High	High
Adaptability	**High**	Low	Low	Low
Stability	High	**Moderate**	High	**Moderate**
Speed	Moderate	Moderate - High	Moderate – high	Low-moderate

	Pump (nm)	Stokes (nm)	Raman (cm^{-1})
Stokes shaping	790	1004-1060	2700-3230
Pump shaping	780-820	1045	2650-3220

Fig. 1. Conceptual and optical designs of TOSS-HS-CARS. (a) Time-frequency distribution diagrams of TOSS, SF, BB, and LS HS-CARS show differences in frequency bandwidth, pulse width, and temporal overlap. (b) Comparison of TOSS, SF, BB, and LS HS-CARS in terms of exposure utility, speed, stability, and adaptability. (c) Optical setup diagram of TOSS-HS-CARS that can perform either shaped-pump or shaped-Stokes operation. The pump (shaped and original) beam is colored in red, and the Stokes (shaped and original) beam is in green. The two pulse shapers (FTPS) have the same optical design with different choices of components. A detailed schematic of the FTPS is shown in the box on the right. The table summarizes the pump and Stokes wavelengths and the range of Raman vibrational frequencies probed by the shaped-pump and shaped-Stokes configurations. HWP, half-wave-plate; PBS, polarization-sensitive beam splitter; PCF, photonic crystal fiber; LP, linear polarizer; QWP, quarter waveplate; GM, galvanometer mirror; DM, dichroic mirror; FTPS, Fourier transform pulse shaper; HPD, hybrid photodetector; CL, cylindrical lens; SLM, spatial-light modulator; ODL, optical delay line.

2. Methods

2.1. Optical design

Figure 1(c) shows the system setup and the detailed design of the pulse shaper. While the two FTPSs were incorporated into the setup for the pump and Stokes, they were not operated simultaneously, which will be discussed in the later sections. The pump beam is sourced from the tunable output of the laser (InsightX3+, 80 MHz, Spectra-Physics) and the Stokes beam is sourced from the fixed output of the laser (centered at 1045 nm). The base design combines the pump and Stokes beam with a dichroic mirror (DM, FF880-SDi01, Semrock) with independent optical delay lines for the pump and the Stokes beams. Both have independent polarization

Optics EXPRESS

control using a pair of half-wave plates to match their optical axes at the sample plane. The combined beams were scanned using a pair of galvanometer mirrors (GMs, 6220 H, Cambridge Technology), and were focused onto the sample by the objective (XLPLN25XWMP2, Olympus Corporation). The CARS signals were detected by a hybrid photodetector (HPD, R10467U-40, Hamamatsu) after collection in the epi direction and after passing through spectral filters.

In the Stokes pulse-shaping scheme, 1.3 W of 1045 nm output was coupled into a photonic-crystal fiber (PCF, LMA-PM-10, NKT Photonics) to generate a broadband continuum of 200 nm bandwidth (base-to-base). The output of the PCF was shaped by a custom pulse-shaper which can perform high-precision amplitude and phase shaping independently, consisting of a diffraction grating (263232-8112-024, 900 lines/mm, blazed at 1000 nm, Zeiss) that separates the spectrum spatially, an achromatic half-wave plate (AHWP05M-980, Thorlabs) to optimize the input polarization for maximum SLM efficiency, a 75-mm cylindrical lens (ACL-254-75-B, Thorlabs) to collimate each spectral component, and a 2D SLM (SLM 200, 1920×1200 pixels, Santec). This particular combination of components was chosen such that the 200-nm bandwidth of the continuum spans the longer edge of the SLM, corresponding to about 0.1 nm (~1 cm-1) per pixel. A half-wave plate placed at the input of the pulse shaper optimizes the polarization of the beam for maximum efficiency of diffraction from the grating. The shaped Stokes beam was then combined and coupled back into the original Stokes beam path (from the output of the laser). An optical delay line (ODL) was inserted between the PCF and the FTPS to delay the shaped Stokes beam by 1 laser pulse period (12.5 ns for 80 MHz) compared to the pump. In the Stokes-shaping scheme, the pump power at the sample arm was around 15 mW and each spectral window of Stokes was around 1~2 mW. The shaped-Stokes method was preferred because the CARS signal strength is proportional to the square of the pump power.

The pump-shaping scheme has a similar design where the pump frequencies were generated by another PCF (LMA-PM-5, NKT Photonics) pumped at 0.8 W at 800 nm [38,39] and shaped using a custom pulse shaper with a similar design using a 600 lines/mm grating, blazed at 775 nm (Zeiss), an achromatic HWP, a 50-mm cylindrical lens (ACL-254-50-B, Thorlabs), and a 2D SLM (Meadowlark, 512×512 pixels). This particular combination of components was chosen such that the 150-nm base-to-base bandwidth of the continuum spans one edge of the SLM, corresponding to an average of 0.3 nm (~4 cm-1) per pixel. The shaped pump beam is temporally delayed by one laser period relative to the 1045-nm output of the laser. The description of the optical design and instrumentation in the shaped-pump and shaped-Stokes schemes is included in Supplement 1, Table S1.

2.2. Optimization and calibration of FTPS

To use a pulse shaper for HS-CARS, there are four essential optimization and calibration steps: 1) optimizing the spectral filtering characteristics in the FTPS, 2) optimizing the beam profile along the beam path after the FTPS for different spectral and temporal profiles, 3) calibrating a look-up table to accommodate the spectrally-dependent voltage-to-phase modulation of the liquid crystals, and 4) matching the spectral and temporal characteristics of the pump and Stokes beams for optimal HS-CARS performance. The first step is to optimize the spectral filtering performance using the 2D SLM. The principle of amplitude modulation using a 2D SLM utilizes constructive and destructive interference of each spectral component of the beam by imparting periodic patterns in a direction orthogonal to the axis of spectral spreading [23]. In our setup, the different frequencies were horizontally displaced on the SLM along its longer axis. By vertically encoding a phase grating on each column, the amplitude of each frequency component can be independently modulated in either a zero- or first-order diffracted beam [23]. The phase grating is defined as a periodic rectangular function with an amplitude (A) and width (P/2). We adopted the zero-order approach for simplicity. The incident beam and the diffracted output were slightly vertically displaced (<1 rad). In this approach, the output intensity of a

Optics EXPRESS

certain frequency component ($I_0(\omega)$) is related to the amplitude ($A(\omega)$) of the phase grating by: $I_0(\omega) \sim \cos^2\left(\frac{A(\omega)}{2}\right)$. It is clear that an amplitude of π results in the maximum modulation in contrast to an amplitude of 0. The overall efficiency also depends on the period of the phase grating, and it varies with different SLMs. After experimentally optimizing the efficiency, in the Stokes FTPS, the SLM can achieve over 90% modulation depth over the entire 200-nm bandwidth. Examples of amplitude modulation results can be found in Supplement 1, Fig. S1. After amplitude modulation is optimized, the pulse shaper is capable of selecting frequency components by suppressing the unwanted frequencies. This was used to accurately determine the wavelength-to-pixel relationship. All spectral measurements during the calibration were performed using a spectrometer (USB4000, Ocean Optics).

The next step is to optimize the beam profile at the output such that the beam maintains a radially symmetric Gaussian-like shape and holds a stable centroid location during the wavelength sweeping, which is critical for HS-CARS since the spatial overlap of the pump and Stokes directly affects the signal strength. This is mainly achieved by fine-tuning the optical alignment of the grating, rotation, position, and axis of the cylindrical lens, and the tip, tilt, and position of the SLM, and by monitoring the beam profile using a camera (MQ013CG-ON-S7, XIMEA) in the far field after different arbitrary distances of propagation. We tested the stability of the spatial profile during wavelength sweeping and amplitude modulation (Visualization 1 and Visualization 2). The shifts in centroid location and the Gaussian-fitted FWHM were plotted in Supplement 1, Fig. S2. Overall, less than 10% changes were observed for both the shaped pump and the shaped Stokes beam. The SLM in the Stokes FTPS also has a wavefront correction feature to help minimize the wavefront distortion at the far field by providing a flat pulse shaper profile. The beam size and shape were also adjusted using a 4f telescope at the output of the pulse shaper to ensure that the shaped beam had a slightly smaller beam diameter than the direct output of the laser, and consequently, a lower numerical aperture to increase the tolerance of alignment in scattering samples by having a slightly larger depth of focus.

After the alignment was optimized, we then calibrated a look-up table (LUT) for the SLM pixel intensity value and the desired phase value. Note that the commercially available SLMs have built-in LUTs. However, the phase response of the liquid crystal is subject to various external factors such as age, temperature, and humidity [40]. Most importantly, it is also optical-frequency-dependent and spatially nonuniform [40–42]. It was therefore important to perform LUT calibration on the SLMs to ensure an accurate phase response across the full bandwidth. We used the amplitude modulation principle described above and measured modulation efficiency by differing the value of A (in pixel intensity) about a fixed center set to 2^{b-1}, where b is the bit depth of the SLM. For example, for a 10-bit SLM, a linear LUT should map pixel intensity values of 0-1024 to phase values of 0-2π. Ideally, if the phase grating amplitude, A, were varied from 0 to 1024, the intensity response would follow a $\cos^2\phi$ curve where ϕ ranges from 0 to π. However, the response may not be linear and may vary with frequency and spatial location on the SLM. Figure S3 shows an example of the mismatched measured modulation effect and the ideal $\cos^2\phi$ response. By inverting the modulated intensity using an inverse cosine and interpolating it for every unique pixel intensity value in MATLAB 2022 (fitted to "spline"), one can obtain a LUT for mapping the regular grey values (pixel values) to the actual/desired phase values for every wavelength. Figure S3 also shows examples of the fitting results on the pump FTPS SLM and the Stokes PS SLM, compared to a linear fit. The most rigorous way to account for spatial and frequency dependence is to do the LUT calibration on each pixel for several wavelength sub-bands within the spectral range of operation. However, in our configuration, the frequency is the same for each column on the SLM, so the LUT calibration was performed on each column using a broadband beam and capturing the intensity trends using a spectrometer (USB4000, Ocean Optics). The LUT calibration result for the Stokes-shaping SLM is shown in Fig. 2(b). Once the LUT was determined, we repeated the first step to check for differences since at the very

Optics EXPRESS

beginning we assumed a linear phase response. Since each LUT curve was close to a linear fit, it did not affect the spectral filtering efficiency or the wavelength-to-pixel calibration significantly. However, the effect of the LUT calibration affected the efficiency of phase modulation much more profoundly. The spatial variance of the LUT curve affected the beam profile but it was optimizable by fine adjustment of the optical alignments.

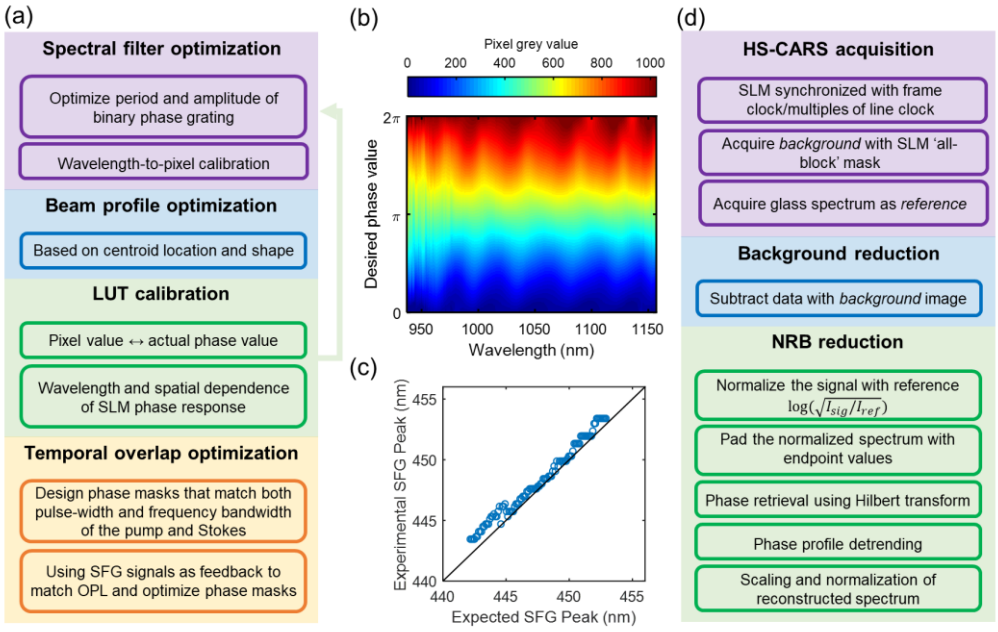

Fig. 2. TOSS-HS-CARS optimization, calibration, data acquisition, and processing. (A) Major calibration steps include optimizing spectral filtering using the amplitude modulation capability of a 2D SLM, wavelength-to-pixel calibration, beam profile optimization, LUT calibration and validation, and pump-Stokes temporal overlap optimization using SFG response. (B) LUT for the Stokes PS SLM. (C) Experimental SFG peak locations in the shaped-Stokes scheme. (D) Major steps for data acquisition and postprocessing include frame/sub-frame synchronization, background reduction, and non-resonant background reduction based on the Kramers-Kronig relation.

Next, to achieve the temporal overlap of the pump and the Stokes, as shown in Fig. 1(a), both the pump and Stokes should have the same temporal pulse width and the same spectral frequency bandwidth. Ideally, they should also have the same dispersion profile for maximum spectral resolution. In the Stokes-shaping scheme, the $1/e^2$ bandwidth of the pump centered at 790 nm was measured to be 10 nm (160 cm^{-1}), which corresponds to an 18 nm bandwidth for the Stokes beam centered at 1045 nm. Initially, a quadratic phase function $\phi(\omega) = A_2(\omega - \omega_0(\omega))^2$ with the A_2 being -2000 fs^2 and a center frequency ω_0 at 1045 nm was applied along the frequency axis (i.e., the horizontal axis of the SLM) to achieve the same pulse width of the pump beam, measured to be 850 fs FWHM at the sample plane using an autocorrelator (Carpe, APE). To temporally overlap the pulses of the pump and shaped Stokes, the sum-frequency generation (SFG) response from a beta barium borate (BBO) crystal was recorded using a spectrometer. SFG was maximized first at the selected band (18-nm $1/e^2$ bandwidth) centered at 1045 nm. The goal was to achieve a linear spectral response of the SFG spectrum and a constant SFG amplitude while sweeping Stokes frequencies. We found that fine adjustment of the ω_0 for each selected narrow band resulted in a more uniform SFG amplitude and more linearly spaced peak SFG frequency. This is

Optics EXPRESS

equivalent to adding a frequency-dependent linear term to the phase modulation function, which corresponds to a frequency-dependent temporal delay. For each ω in the bandwidth, the SFG response was acquired for a series of ω_0 over a large range. The $\omega_0(\omega)$ frequencies were chosen such that the overlap between the expected SFG response, which was modeled as a Gaussian spectrum with a linewidth of around 80 cm^{-1} calculated from the measured line widths of the pump and Stokes beams, and the measured SFG response, was maximized. Figure 2(c) shows an example of experimental SFG peak locations during the frequency sweep as compared to calculated peak locations, which were observed to follow an overall linear trend. In the time domain, this is equivalent to tuning the optical path length delay for each optical band; however, TOSS-HS-CARS achieves this without any moving parts.

Prior to collecting data on each day of operation, the output of the Stokes PCF was first set to 650 mW with maximum coupling efficiency. The optical delay unit in the pump was then adjusted such that the SFG spectrum from the BBO crystal at the sample plane at the phase mask passing 1030 ± 9 nm had the highest peak and was centered at 447 nm (when the pump beam was centered at 790 nm). The procedures described here for the shaped-Stokes TOSS-HS-CARS were repeated for the shaped-pump TOSS-HS-CARS with the appropriate parameters for each instrument.

2.3. Acquisition and postprocessing

A series of patterns were generated for sweeping the Stokes beam wavelength across the spectral range, where the passband consisted of a quadratic function along the horizontal direction with the previously calibrated values of A_2 and $\omega_0(\omega)$ and the stop band consisted of phase grating with an amplitude of π centered at 2^{b-1}. All the patterns were initially computed as phase functions, digitally wrapped and confined to a range of $-\pi$ to π, and then converted to pixel intensity values using the calibrated look-up table for each spectral component. An example of a pattern is shown in Supplement 1, Fig. S3(b). Image acquisition was performed using custom LabVIEW software (National Instruments) and a data acquisition and timing module (PCIe 6356, NI), based on the setup described in [43,44]. The SLM can be synchronized with an external trigger for sweeping different patterns, advertised at up to 60 Hz. However, practically, we observed that the slew rate for the full range was closer to 100 ms. The digital triggers for every frame or a set of a few lines were exported from the timing module to the trigger port of the SLM. The predominant acquisition method used in this work was x-y-f, where the SLM was synchronized to the frame clock of image acquisition which was typically ~1 Hz. The trigger was advanced from the actual start of the frame by ~100 ms to account for the slew in changing the pattern. Note that this slew rate is different from the response time of the LCs.

In the Stokes-shaping scheme, the series of patterns not only included the phase masks for sweeping the Stokes wavelengths from 1000 nm to 1060 nm, but also included a phase mask passing the entire 1000-1060 nm band compressed to around 200 fs (referred to as "all-pass mask"), and one suppressing the entire band (referred to as "all-block mask"). The "all-pass" mask was mainly used for adjusting the focus based on structural features and signal intensities. The "all-block" mask was used to remove background signals within the emission band generated by the pump alone. We assumed that most of the signals detected in the same spectral window were either autofluorescence signals excited by the pump beam or the pump beam leaking into the detector despite the high-efficiency cutoff filters. The pump beam was set at 790 nm and around 10–20 mW at the sample plane, whereas each sweep of the Stokes beam only had 1-2 mW at the sample plane. The image generated by the all-pass mask was used to visualize the spectrally-agnostic structures of the sample. The spectra from a clean block of glass collected using the same phase masks under the same imaging conditions were used as the reference for NRB reduction in the processing.

Optics EXPRESS

After the acquisition, the background image acquired using the all-block mask was first subtracted from all the HS-CARS images. For the spectroscopic characterization of pure solutions, since the field of view (FOV) is mostly uniform, the mean intensity from the image at each frequency was used to construct the raw signal spectrum. For NRB reduction, we adopted the phase-corrected KK-relation phase retrieval algorithm [10]. The raw signal spectrum (I_{sig}) was first normalized by the glass spectrum (I_{ref}): $A_{sig}(\omega) = \log\left(\sqrt{I_{sig}(\omega)/I_{ref}(\omega)}\right)$. To reduce the edge artifacts from the Hilbert transform, we padded the spectrum with end-point values to extend the spectrum by 10 times in length. After Hthe ilbert transform of the normalized signal, $A_{sig}(\omega)$, the imaginary part was used as the reconstructed phase of the CARS signals. We then performed a first-order detrending on the retrieved phase to correct the phase error, with the assumption that the phase has a zero baseline [9]. The baseline-corrected phase was then used to reconstruct the CARS spectrum with intensity rescaling by $\sqrt{I_{sig}(\omega)/I_{ref}(\omega)}$. A first-order amplitude baseline detrending was optionally performed. All the processing was performed post-acquisition using MATLAB R2022b and the standard detrending function.

2.4. Chemical compound imaging

Approximately 1 mL of pure solutions of dimethyl sulfoxide (DMSO), methanol, glycerol, ethanol, and water were separately placed in clean cover glass-bottomed Petri dishes (P35G-0-14-C, MatTek) prior to imaging. A polydimethylsiloxane (PDMS) sample was prepared by mixing PDMS with room-temperature vulcanizing agents (RTVA for curing and RTV-B for crosslinking) in the ratio of 100:10:1 and set for several hours to form a stable gel at room temperature. The glass background was collected from a glass microscope slide (Premium microscope slide superfrost, 12-544-7, Fisher Scientific). The spectra for all solutions, gels, and glass were collected in the epi direction from a depth of 10-20 µm below the surface. All spectra were acquired as $256 \times 256 \times 103$-pixel data cubes with 12.5 µs exposure time per pixel, where the first two dimensions indicate the transverse image size and the last dimension indicates the number of spectral components collected. The 103 patterns included 101 patterns of the Stokes wavelength swept at an interval of 5.4 cm^{-1} between 2690 cm^{-1} and 3228 cm^{-1}, the all-pass phase mask, and the all-block phase mask.

2.5. Mouse tissue imaging

A mouse was euthanized by CO_2 asphyxiation and tissues were surgically resected and placed in an imaging dish with a clear cover-glass bottom containing approximately 100 µL of freshly prepared phosphate-buffered saline. The dishes were placed on ice and the tissues were imaged with a few hours of extraction. All animal procedures were conducted in accordance with a protocol approved by the Illinois Institutional Animal Care and Use Committee at the University of Illinois at Urbana-Champaign. The images were either collected as $256 \times 256 \times 103$-pixel data cubes in the same configuration as the data for the pure compounds, or as 6×3 tiles of $256 \times 256 \times 33$-pixel data cubes each (10 cm^{-1} spacing between 2750 cm^{-1} and 3050 cm^{-1}, the all-pass phase mask, and the all-block phase mask). Non-resonant background reduction was performed using the same algorithm described in section 2.3. To generate lipid-to-protein maps, normalized gaussian windows centered at 2850 cm^{-1} (lipid) and 2950 cm^{-1} (protein) with a bandwidth of 40 cm^{-1} (system's spectral resolution) were used to filter out the CARS signal contributions from lipids and proteins.

Optics EXPRESS

3. Results

3.1. Spectroscopic characterization of homogenous chemical compounds

First, we show that the Stokes-shaping HS-CARS can be used to characterize different chemical compounds, including dimethyl sulfoxide (DMSO), methanol, ethanol, cured polydimethylsiloxane (PDMS), and glycerol, where the spectrum from the glass was used as the reference for NRB reduction. The Stokes central wavelength was swept from 1004 nm to 1060 nm with an interval of 0.5 nm, which resulted in Raman spectra from 2690 cm^{-1} to 3228 cm^{-1}. The results were compared to the spontaneous Raman spectra as shown in Fig. 3. The left column shows the raw data before NRB reduction, the middle column shows the KK-corrected CARS spectra and the right column shows the spectrum collected from a spontaneous Raman confocal microscope [45]. Even before NRB reduction, the CARS spectra appear more similar to the spontaneous Raman spectra despite some differences in the shape, peak location, and bandwidth of individual peaks. These spectral features were more like spontaneous Raman scattering spectra after NRB removal. For instance, the two peaks of different intensities of DMSO, the two peaks of similar intensities in methanol, the three peaks of different intensities of ethanol, the single narrow peak of PDMS, the single broad peak of glycerol, and the lack of any distinct vibrational peaks of glass were all recovered accurately with our technique after NRB removal.

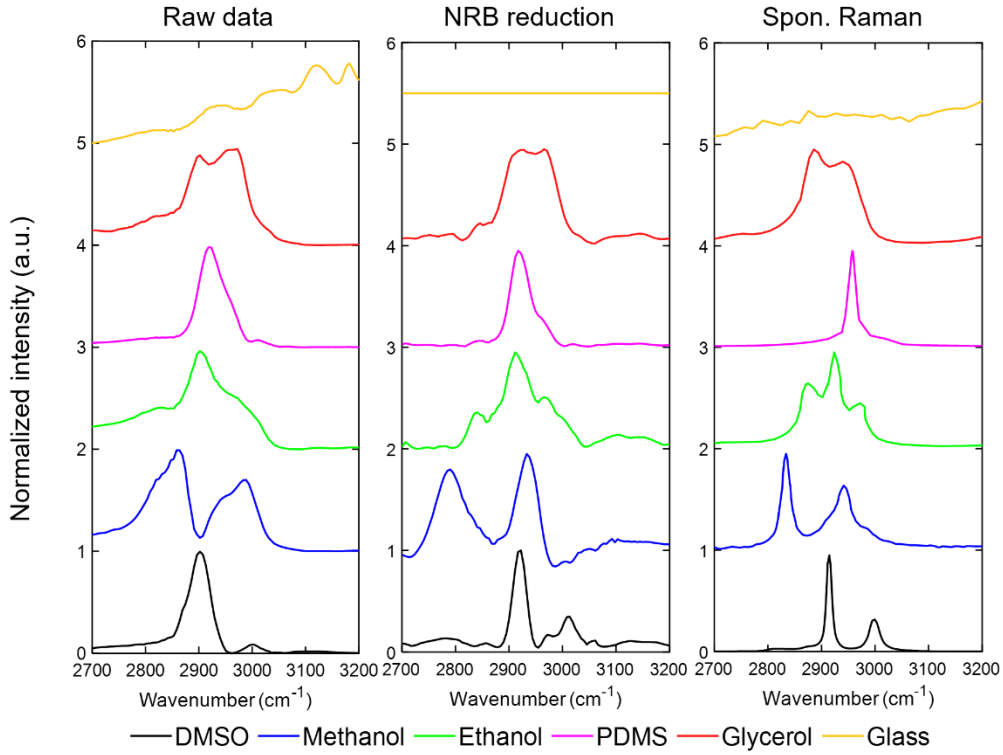

Fig. 3. Characterization of chemical compounds by shaped-Stokes HS-CARS, including DMSO, methanol, ethanol, PDMS, glycerol, and glass. The left column contains spectra obtained from the mean intensity of each frame acquired at each shaped-Stokes wavelength, referred to as the "raw data". The middle column contains the reconstructed spectra after KK-relation-based NRB reduction. The right column contains the spontaneous (Spon.) Raman spectra of the compounds. All spectra were normalized for visualization.

Optics EXPRESS

For DMSO (Fig. 3, black trace), the strongest peak in the spectrum before correction was located at 2902 cm^{-1} with a FWHM of 40 cm^{-1}. The theoretical spectral resolution was calculated to be around 34 cm^{-1} with the Stokes-shaping scheme, assuming pure second-order dispersion [46]. The experimental data showed good accordance with the theoretical calculation. The corresponding peak in spontaneous Raman is located at 2915 cm^{-1} with a FWHM of around 10 cm^{-1}. The peak shift towards lower frequency could be due to the interference of the resonant signals and the NRB [3]. After NRB reduction the major peak of DMSO was relocated at 2912 cm^{-1} with a FWHM 30 cm^{-1} with the second peak at 3000 cm^{-1} appearing more significant. The intensity ratio between the two peaks was similar to that in the spontaneous Raman spectrum. For methanol (blue trace), two major peaks were observed at 2780 cm^{-1} and 2924 cm^{-1} with FWHM of around 45 cm^{-1}, which were slightly shifted from the peaks at 2829 cm^{-1} and 2940 cm^{-1} observed from spontaneous Raman imaging. For ethanol (green trace), while only one peak was observed in the raw data, three distinct peaks can be identified after NRB reduction. These peaks were also shifted towards lower wavenumbers as compared to the spontaneous Raman data and had different intensity trends. A similar peak shift was also observed for PDMS (purple trace) towards slightly lower wavenumbers. For glycerol, no major peaks were expected but the FWHM of the spontaneous Raman spectrum was around 110 cm^{-1} centered at 2915 cm^{-1}. Our measured spectrum of glycerol had a FWHM of around 110 cm^{-1} centered at around 2940 cm^{-1}(both before and after NRB reduction), which was larger than the system spectral resolution. However, we could not accurately resolve the peaks at 2890 cm^{-1} and 2940 cm^{-1} as the spontaneous Raman. Glass signals had a slight increase over this range of wavenumbers, and the NRB reduction gave results of zero amplitude since it assumed that there should not be resonances in the glass.

3.2. Microscopy of biological samples

We demonstrate the ability of shaped-Stokes HS-CARS to capture chemical information in *ex vivo* biological tissue. Figure 4 shows HS-CARS normalized intensity images averaged over the entire frequency sweeping range (grayscale, left column), the corresponding normalized lipid/protein ratio maps (blue-to-red map, center column), and representative spectra from regions of interest (ROI) (right column). The images in Fig. 4(a) were acquired from a subcutaneous region in the mouse skin. A few small adipocytes (5-25 μm diameter) can be identified as the regions with the highest lipid-to-protein ratios. The protein-rich regions consisted of collagen fibers that were not resolved in the CARS image but were apparent in the spectrally adjacent autofluorescence channel (Supplement 1, Fig. S4). Differences in the CARS spectrum can be identified in the selected ROIs between the protein-rich and lipid-rich regions. Lipids are expected to have a vibrational peak frequency in the CH-stretching region, located around 2850 cm^{-1}, and proteins at 2950 cm^{-1} [47–49]. ROI 1a was selected inside an adipocyte and had 3-fold greater signals in the 2800 cm^{-1}–2900 cm^{-1} range compared to the 2900 cm^{-1} -3000 cm^{-1} range, whereas ROI 2a had constantly increased signals over 2800 cm^{-1} -3000 cm^{-1}, which was selected in the collagen-rich region. ROI 1b within the muscle tissue in Fig. 4(b) had gradually increasing signals over 2800 cm^{-1} -3000 cm^{-1} that were similar to the ROI 2a. In contrast, ROI 2b was selected from a lipid droplet that had a dip in the signals at around 2940 cm^{-1}. Also, the overall signal strength was lower compared to the protein-rich regions (e.g., ROI 2a, 1b). In the liver tissue shown in Fig. 4(c) with lipid droplets scattered across the FOV, ROI 1c was selected from the hepatocyte-rich region, which could be observed in the autofluorescence channel (Fig. S4). The CARS spectrum at ROI 1c showed an increase in signals from 2750 cm^{-1} that peaked at 2950 cm^{-1}, which indicates that it is protein-rich. ROI 3c was selected from one of the lipid droplets and had significantly stronger signals in the range of 2850 cm^{-1} - 2900 cm^{-1}, which validates that it is lipid-rich.

Optics EXPRESS

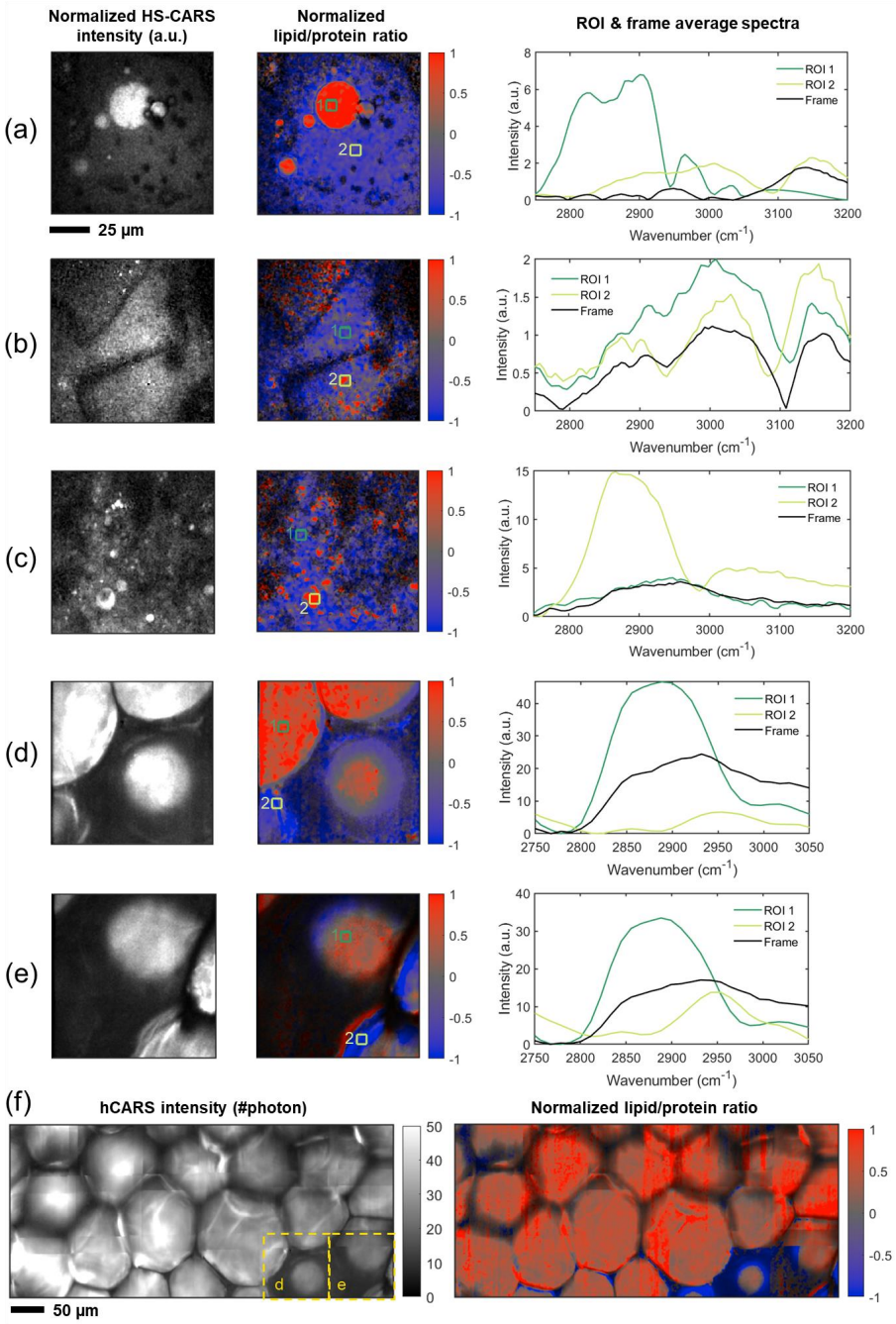

Fig. 4. Shaped-Stokes HS-CARS of *ex vivo* mouse tissue showing an intensity image (left column), a normalized lipid-to-protein ratio map (middle column), and average spectra from selected regions-of-interest (ROI) and the entire frame (right column). (a) Subcutaneous region in the mouse skin (abdominal region) with adipocytes and collagen fibers. (b) Muscle with lipid droplets. (c) Liver with lipid droplets. (d-f) A subcutaneous region in the skin was imaged with 31 different Stokes wavelength bands, covering a slightly narrower wavenumber range from 2750 cm^{-1} to 3050 cm^{-1}. (f) Large area mosaic showing multiple adipose, and (d, e) selected FOVs of about 100 μm × 100 μm in size. (a-e) images were on the same scale (25 μm scale bar) and selected ROIs were all around 6 μm × 6 μm.

Optics EXPRESS

To demonstrate the fidelity of our system, we also captured a large area mosaic of subcutaneous region within the mouse skin, with sparser spectral sampling ($10\,cm^{-1}$) over a shorter range ($300\,cm^{-1}$) (Fig. 4(f)). Selected FOVs that contain both lipid-rich and protein-rich structures are shown in Fig. 4(d, e). In contrast to the lipid content, the membranes of the large adipocytes were highlighted in blue in the lipid-to-protein map. Each hyperspectral data cube shown in this dataset was captured within four minutes, limited by the exposure time (12.8 μs) for a sufficient number of photons collected from the samples.

4. Discussion

In this paper, we presented a novel concept for HS-CARS that had no moving parts, was adaptable to various acquisition schemes, and utilized the exposure on the sample effectively with a customized and carefully calibrated FTPS. Several considerations led to the proposed temporally optimized and spectrally shaped (TOSS) HS-CARS method and the presented optical design. First is the preference of demonstrating this concept on CARS over stimulated Raman scattering (SRS) microscopy. Although SRS does not have an NRB and could be computationally simpler and more accurate than CARS, it usually requires modulation of the excitation beam [50,51] which introduces more instrumentation complexity, power loss, and lower compatibility within a multimodal imaging system, especially in the epi detection configuration. Nonetheless, the proposed method can also be used in hyperspectral SRS imaging and generalized further to other spectroscopic techniques. Second, we demonstrated the feasibility of pump-shaping TOSS-HS-CARS (Supplement 1, Fig. S5) but chose the Stokes-shaping method as the predominant demonstration in the paper. While a part of the better performance of the Stokes-shaping scheme can be attributed to the differences in optical components that affected the performance of the pulse shapers themselves, there is also a physical basis for this choice. CARS signal strength increases quadratically with the pump beam intensity and linearly with Stokes beam intensity; thus, a powerful and stable pump source is favorable. Moreover, the pump wavelength is also tunable within our laser, which adds more flexibility to selecting the targeted wavenumber range. By tuning the pump wavelength, finger-print region CARS is also feasible with minimal adjustment of the detection optics. The Stokes can be obtained by either the fiber continuum source pumped by the tunable or fixed output of the laser. However, we also anticipated challenges with the current setup to perform high-quality finger-print CARS measurements, including insufficient power efficiency and detection efficiency at CARS wavelengths. Furthermore, the pump beam can also be used to simultaneously excite two-photon fluorescence and second-harmonic generation, which can provide different contrasts from the same FOV in the sample and even simultaneously. Third, as previously mentioned in the Introduction, there are a few commercially available FTPS devices based on 2D SLMs. Many have restricted access to the SLM to impart the customized patterns utilized in this study and are five to ten times more expensive. Nonetheless, FTPSs have increasing utility for multiphoton microscopy [6,52] and TOSS-HS-CARS can integrate easily into these existing modules.

Our results demonstrated HS-CARS using a frame-by-frame acquisition scheme, which is known to be subject to motion-induced distortion [53]. We observed a lateral shift of 1~2 μm between the first and last frame of the data cube (acquired within 120 seconds) due to tissue relaxation. Although this shift is small (< 5 pixels) and was compensated with a lateral median filter that was applied postprocessing, it can rigorously be corrected by image registration. However, the acquisition method is not limited to frame-by-frame capture of spectroscopic data. While the SLMs used in this study had a slew rate of tens of milliseconds that restricted the operational speed to <60 Hz, ultrafast SLMs capable of 200 Hz operation are commercially available. The feasibility of synchronizing the SLM to multiples of the line clock has been shown in Supplement 1, Fig. S6. This can be particularly useful for the fast characterization of pure chemical compounds or uniform samples. While pixel-to-pixel sweeping of the beams

Optics EXPRESS

is theoretically feasible, the millisecond-scale pixel dwell time that it needs can be more prone to photodamage. Besides flexible acquisitions, the choice of shaped-Stokes wavelengths can be flexible according to users' needs. For example, one can easily choose to only collect data in the lipid region and the protein region for fast characterization of the lipid-to-protein ratio. The adaptability and flexibility of this method are not limited to data acquisition. We also experimented with Stokes-shaping HS-CARS in the femtosecond regime (Fig. S7), in which case simultaneous and optimized excitation of other multiphoton processes is possible.

While our proposed TOSS-HS-CARS technique has noteworthy versatility and potential, it also has some limitations and challenges. First, the spectral resolution reported in this paper was around $40\,\mathrm{cm}^{-1}$(represented by the FWHM of the DMSO peak at $2915\,\mathrm{cm}^{-1}$, which is not comparable to some of the high-resolution CARS systems [54,55]. This was limited by the pulse width of the pump and the Stokes beams, which was about 850 fs at the sample plane. Increasing the pulse width of both beams by adding more dispersion can certainly improve the spectral resolution but this will degrade other multiphoton signals and thus impede the simultaneous detection of multiple channels. In the future, we intend to implement a high-resolution TOSS-HS-CARS to better resolve molecule resonances (typically $\sim 10\,\mathrm{cm}^{-1}$ [1]) by increasing the chirp of both beams and incorporating higher-order dispersion parameters into the model for generating the SLM phase patterns. Users will be able to switch between high-resolution and simultaneous multi-channel operation modes for different needs and applications. Second, the range of vibrational frequencies probed in one HS measurement in our setup is mainly limited by the spectral bandwidth and signal strength of the PCF output, and the wavelength-dependent efficiency of the SLM and the grating in the FTPS. Enhancing these components through customization is an option, but opting for commercially available products offers a more cost-effective solution. Third, even though the broadband continuum generated by PCF has been demonstrated as a stable source for many spectroscopy and microscopy applications [6,56–58], the fluctuations of the spectral shape can cause inaccuracy of the CARS measurement. We can monitor the changes in the shaped beam spectral amplitude and the temporal and spatial overlaps through the SFG measurement. Lastly, the implementation of FTPS and PCF and the calibration procedures add complexity to the HS-CARS measurements and thus this approach is better suited for systems with multimodal abilities, systems that require high mechanical stability, and studies that demand high exposure utility.

5. Conclusion

TOSS-HS-CARS offers advantages over both SF-HS-CARS and LS-HS-CARS including high exposure utility, and fast and stable operation without any moving parts. The adaptive configurations enable multiple acquisition schemes limited only by the exposure time and the operational characteristics of the optoelectronic components. While we presented TOSS-HS-CARS in three different schemes, Stokes-shaping, pump-shaping, and femtosecond-pulse with two different acquisition modes, there are more possible adaptations of this concept and improvements of the system such as the spectral resolution. Moreover, adaptive acquisition enables better freedom in choosing the optimal point between speed and spectral resolution for simple ratiometric analysis or dynamic imaging applications. We plan to develop these concepts into adaptive acquisition HS-CARS without any significant changes to the optical setup in the future. We believe that TOSS-HS-CARS can enable rapid and specific chemical characterization of biological tissue and other materials with great adaptability and tunability.

Funding. National Institutes of Health (P41EB031772, R01CA213149, R01CA241618, T32EB019944).

Acknowledgments. The authors would like to acknowledge Darold Jr. Spillman for his assistance with purchasing laboratory supplies for this research, and Eric J. Chaney for helping with research animals handling. Besides the major funding sources listed above, L.Y. was supported by UIUC Beckman Institute (Beckman Graduate Student Fellowship),

Optics EXPRESS

and J.E.S. was supported by the UIUC Department of Bioengineering (McGinnis Medical Innovation Graduate Student Fellowship). Additional information can be found at: http://biophotonics.illinois.edu.

Disclosures. A patent has been filed for the fast fluorescence lifetime imaging technique described in this paper (J.E.S., R.R.I., and S.A.B.). An invention disclosure has been submitted for the technique to perform temporal optimization and spectral shaping for hyperspectral coherent Raman microscopy, as described in this paper (L.Y., J.E.S., R.R.I., and S.A.B.). The authors declare that they have no other competing interests.

Data availability. The data that support the findings of this study are available from the corresponding author upon reasonable request and through collaborative investigations. The MATLAB code for the SLM mask generation and CARS processing will be made available in a public repository upon publication and is found in Ref. [59].

Supplemental document. See Supplement 1 for supporting content.

References

1. C. L. Evans and X. S. Xie, "Coherent anti-Stokes Raman scattering microscopy: chemical imaging for biology and medicine," Annu. Rev. Anal. Chem. **1**(1), 883–909 (2008).
2. J. X. Cheng and X. S. Xie, "Vibrational spectroscopic imaging of living systems: An emerging platform for biology and medicine," Science **350**(6264), aaa8870 (2015).
3. J. X. Cheng, "Coherent anti-Stokes Raman scattering microscopy," Appl. Spectrosc. **61**(9), 197A–208A (2007).
4. J. P. Pezacki, J. A. Blake, D. C. Danielson, *et al.*, "Chemical contrast for imaging living systems: molecular vibrations drive CARS microscopy," Nat. Chem. Biol. **7**(3), 137–145 (2011).
5. P. D. Chowdary, Z. Jiang, E. J. Chaney, *et al.*, "Molecular histopathology by spectrally reconstructed nonlinear interferometric vibrational imaging," Cancer Res. **70**(23), 9562–9569 (2010).
6. H. Tu, Y. Liu, D. Turchinovich, *et al.*, "Stain-free histopathology by programmable supercontinuum pulses," Nat. Photonics **10**(8), 534–540 (2016).
7. J. Shi, K. Bera, P. Mukherjee, *et al.*, "Weakly Supervised Identification and Localization of Drug Fingerprints Based on Label-Free Hyperspectral CARS Microscopy," Anal. Chem. **95**(29), 10957–10965 (2023).
8. E. M. Vartiainen, "Phase retrieval approach for coherent anti-Stokes Raman scattering spectrum analysis," J. Opt. Soc. Am. B **9**(8), 1209–1214 (1992).
9. M. T. Cicerone, K. A. Aamer, Y. J. Lee, *et al.*, "Maximum entropy and time-domain Kramers–Kronig phase retrieval approaches are functionally equivalent for CARS microspectroscopy," J. Raman Spectrosc. **43**(5), 637–643 (2012).
10. C. H. Camp Jr, Y. J. Lee, and M. T. Cicerone, "Quantitative, comparable coherent anti-Stokes Raman scattering (CARS) spectroscopy: correcting errors in phase retrieval," J. Raman Spectrosc. **47**(4), 408–415 (2016).
11. T. W. Kee and M. T. Cicerone, "A simple approach to one-laser, broadband coherent anti-Stokes Raman scattering microscopy," Opt. Lett. **29**(23), 2701–2703 (2004).
12. D. Polli, V. Kumar, C. M. Valensise, *et al.*, "Broadband coherent Raman scattering microscopy," Laser Photonics Rev. **12**(9), 1800020 (2018).
13. K. Hashimoto, M. Takahashi, T. Ideguchi, *et al.*, "Broadband coherent Raman spectroscopy running at 24,000 spectra per second," Sci. Rep. **6**(1), 21036 (2016).
14. C. H. Camp Jr, Y. J. Lee, J. M. Heddleston, *et al.*, "High-speed coherent Raman fingerprint imaging of biological tissues," Nat. Photonics **8**(8), 627–634 (2014).
15. S. Bégin, B. Burgoyne, V. Mercier, *et al.*, "Coherent anti-Stokes Raman scattering hyperspectral tissue imaging with a wavelength-swept system," Biomed. Opt. Express **2**(5), 1296–1306 (2011).
16. H. Cahyadi, J. Iwatsuka, T. Minamikawa, *et al.*, "Fast spectral coherent anti-Stokes Raman scattering microscopy with a high-speed tunable picosecond laser," J. Biomed. Opt. **18**(9), 096009 (2013).
17. S. Brustlein, P. Ferrand, N. Walther, *et al.*, "Optical parametric oscillator-based light source for coherent Raman scattering microscopy: practical overview," J. Biomed. Opt. **16**(2), 021106 (2011).
18. C. L. Evans, E. O. Potma, M. Puoris' haag, *et al.*, "Chemical imaging of tissue *in vivo* with video-rate coherent anti-Stokes Raman scattering microscopy," Proc. Natl. Acad. Sci. **102**(46), 16807–16812 (2005).
19. T. Hellerer, A. M. Enejder, and A. Zumbusch, "Spectral focusing: High spectral resolution spectroscopy with broad-bandwidth laser pulses," Appl. Phys. Lett. **85**(1), 25–27 (2004).
20. I. Rocha-Mendoza, W. Langbein, and P. Borri, "Coherent anti-Stokes Raman microspectroscopy using spectral focusing with glass dispersion," Appl. Phys. Lett. **93**(20), 201103 (2008).
21. A. M. Weiner, "Femtosecond pulse shaping using spatial light modulators," Rev. Sci. Instrum. **71**(5), 1929–1960 (2000).
22. A. M. Weiner, D. E. Leaird, J. S. Patel, *et al.*, "Programmable femtosecond pulse shaping by use of a multielement liquid-crystal phase modulator," Opt. Lett. **15**(6), 326–328 (1990).
23. E. Frumker and Y. Silberberg, "Phase and amplitude pulse shaping with two-dimensional phase-only spatial light modulators," J. Opt. Soc. Am. B **24**(12), 2940–2947 (2007).
24. J. C. Vaughan, T. Hornung, T. Feurer, *et al.*, "Diffraction-based femtosecond pulse shaping with a two-dimensional spatial light modulator," Opt. Lett. **30**(3), 323–325 (2005).
25. E. Frumker and Y. Silberberg, "Femtosecond pulse shaping using a two-dimensional liquid-crystal spatial light modulator," Opt. Lett. **32**(11), 1384–1386 (2007).

Optics EXPRESS

26. D. Pestov, V. V. Lozovoy, and M. Dantus, "Multiple Independent Comb Shaping (MICS): Phase-only generation of optical pulse sequences," Opt. Express **17**(16), 14351–14361 (2009).
27. V. Ansari, E. Roccia, M. Santandrea, *et al.*, "Heralded generation of high-purity ultrashort single photons in programmable temporal shapes," Opt. Express **26**(3), 2764–2774 (2018).
28. D. V. Reddy and M. G. Raymer, "Engineering temporal-mode-selective frequency conversion in nonlinear optical waveguides: from theory to experiment," Opt. Express **25**(11), 12952–12966 (2017).
29. J. Schröder, M. A. Roelens, L. Du, *et al.*, "An optical FPGA: Reconfigurable simultaneous multi-output spectral pulse-shaping for linear optical processing," Opt. Express **21**(1), 690–697 (2013).
30. V. V. Lozovoy, I. Pastirk, and M. Dantus, "Multiphoton intrapulse interference. IV. Ultrashort laser pulse spectral phase characterization and compensation," Opt. Lett. **29**(7), 775–777 (2004).
31. B. Xu, J. M. Gunn, J. Cruz, *et al.*, "Quantitative investigation of the multiphoton intrapulse interference phase scan method for simultaneous phase measurement and compensation of femtosecond laser pulses," J. Opt. Soc. Am. B **23**(4), 750–759 (2006).
32. F. Sinjab, Z. Liao, and I. Notingher, "Applications of spatial light modulators in Raman spectroscopy," Appl. Spectrosc. **73**(7), 727–746 (2019).
33. B. M. Davis, A. J. Hemphill, and D. Cebeci Maltaş, "Multivariate hyperspectral Raman imaging using compressive detection," Anal. Chem. **83**(13), 5086–5092 (2011).
34. N. Dudovich, D. Oron, and Y. Silberberg, "Single-pulse coherently controlled nonlinear Raman spectroscopy and microscopy," Nature **418**(6897), 512–514 (2002).
35. H. Frostig, T. Bayer, N. Dudovich, *et al.*, "Single-beam spectrally controlled two-dimensional Raman spectroscopy," Nat. Photonics **9**(5), 339–343 (2015).
36. K. Bae, W. Zheng, and Z. Huang, "Spatial light-modulated stimulated Raman scattering (SLM-SRS) microscopy for rapid multiplexed vibrational imaging," Theranostics **10**(1), 312–322 (2020).
37. C. W. Freudiger, W. Min, G. R. Holtom, *et al.*, "Highly specific label-free molecular imaging with spectrally tailored excitation-stimulated Raman scattering (STE-SRS) microscopy," Nat. Photonics **5**(2), 103–109 (2011).
38. R. R. Iyer, J. E. Sorrells, L. Yang, *et al.*, "Label-free metabolic and structural profiling of dynamic biological samples using multimodal optical microscopy with sensorless adaptive optics," Sci. Rep. **12**(1), 3438 (2022).
39. L. Yang, R. R. Iyer, J. E. Sorrells, *et al.*, "Label-free multimodal polarization-sensitive optical microscope for multiparametric quantitative characterization of collagen," Optica **11**(2), 155–165 (2024).
40. R. Li and L. Cao, "Progress in phase calibration for liquid crystal spatial light modulators," Appl. Sci. **9**(10), 2012 (2019).
41. Z. Zeng, Z. Li, F. Fang, *et al.*, "Phase compensation of the non-uniformity of the liquid crystal on silicon spatial light modulator at pixel level," Sensors **21**(3), 967 (2021).
42. T. Zhao, J. Liu, X. Duan, *et al.*, "Multi-region phase calibration of liquid crystal SLM for holographic display," Appl. Opt. **56**(22), 6168–6174 (2017).
43. J. E. Sorrells, R. R. Iyer, L. Yang, *et al.*, "Single-photon peak event detection (SPEED): a computational method for fast photon counting in fluorescence lifetime imaging microscopy," Opt. Express **29**(23), 37759–37775 (2021).
44. J. E. Sorrells, R. R. Iyer, L. Yang, *et al.*, "Computational Photon Counting Using Multithreshold Peak Detection for Fast Fluorescence Lifetime Imaging Microscopy," ACS Photonics **9**(8), 2748–2755 (2022).
45. John Wiley & Sons, Inc. SpectraBase; https://spectrabase.com/ (accessed 10/4/2023).
46. M. Mohseni, C. Polzer, and T. Hellerer, "Resolution of spectral focusing in coherent Raman imaging," Opt. Express **26**(8), 10230–10241 (2018).
47. S. Oh, C. Lee, W. Yang, *et al.*, "Protein and lipid mass concentration measurement in tissues by stimulated Raman scattering microscopy," Proc. Natl. Acad. Sci. **119**(17), e2117938119 (2022).
48. D. Lin-Vien, N. B. Colthup, W. G. Fateley, *et al.*, *The handbook of infrared and Raman characteristic frequencies of organic molecules*, (Elsevier, 1991).
49. N. Huang, M. Short, J. Zhao, *et al.*, "Full range characterization of the Raman spectra of organs in a murine model," Opt. Express **19**(23), 22892–22909 (2011).
50. F. Hu, L. Shi, and W. Min, "Biological imaging of chemical bonds by stimulated Raman scattering microscopy," Nat. Methods **16**(9), 830–842 (2019).
51. C. W. Freudiger, W. Min, B. G. Saar, *et al.*, "Label-free biomedical imaging with high sensitivity by stimulated Raman scattering microscopy," Science **322**(5909), 1857–1861 (2008).
52. S. You, H. Tu, E. J. Chaney, *et al.*, "Intravital imaging by simultaneous label-free autofluorescence-multiharmonic microscopy," Nat. Commun. **9**(1), 2125 (2018).
53. D. Fu and X. S. Xie, "Reliable cell segmentation based on spectral phasor analysis of hyperspectral stimulated Raman scattering imaging data," Anal. Chem. **86**(9), 4115–4119 (2014).
54. J. X. Cheng, A. Volkmer, L. D. Book, *et al.*, "An epi-detected coherent anti-Stokes Raman scattering (E-CARS) microscope with high spectral resolution and high sensitivity," J. Phys. Chem. B **105**(7), 1277–1280 (2001).
55. T. Gottschall, T. Meyer, M. Baumgartl, *et al.*, "Fiber-based optical parametric oscillator for high-resolution coherent anti-Stokes Raman scattering (CARS) microscopy," Opt. Express **22**(18), 21921–21928 (2014).
56. H. Kano and H. O. Hamaguchi, "Ultrabroadband (> 2500cm− 1) multiplex coherent anti-Stokes Raman scattering microspectroscopy using a supercontinuum generated from a photonic crystal fiber," Appl. Phys. Lett. **86**(12), 1 (2005).

Optics EXPRESS

57. Y. Shen, A. A. Voronin, A. M. Zheltikov, *et al.*, "Picosecond supercontinuum generation in large mode area photonic crystal fibers for coherent anti-Stokes Raman scattering microspectroscopy," Sci. Rep. **8**(1), 9526 (2018).
58. Y. Wang, Y. Zhao, J. S. Nelson, *et al.*, "Ultrahigh-resolution optical coherence tomography by broadband continuum generation from a photonic crystal fiber," Opt. Lett. **28**(3), 182–184 (2003).
59. Y. Wang, Y. Zhao, J. S. Nelson, *et al.*, "Ultrahigh-resolution optical coherence tomography by broadband continuum generation from a photonic crystal fiber," Github (2003) https://github.com/Biophotonics-COMI/TOSS-CARS.